Original Paper

A new interacting capillary bundle model on the multiphase flow in micropores of tight rocks

Wen-Quan Deng, Tian-Bo Liang [*], Wen-Zhong Wang, Hao Liu, Jun-Lin Wu, Fu-Jian Zhou

National Key Laboratory of Petroleum Resources and Engineering, China University of Petroleum (Beijing), Beijing, 102249, China

ABSTRACT

Surfactants are widely used in the fracturing fluid to enhance the imbibition and thus the oil recovery rate. However, current numerical models cannot capture the physics behind capillary imbibition during the wettability alteration by surfactants. Although the interacting capillary bundle (ICB) model shows potential in characterizing imbibition rates in different pores during wettability alteration, the existing ICB models neglect the influence of wettability and viscosity ratio on the imbibition behavior, making it difficult to accurately describe the oil–water imbibition behavior within the porous media. In this work, a new ICB mathematical model is established by introducing pressure balance without assuming the position of the leading front to comprehensively describe the imbibition behavior in a porous medium under different conditions, including gas–liquid spontaneous imbibition and oil–water imbibition. When the pore size distribution of a tight rock is known, this new model can predict the changes of water saturation during the displacement process in the tight rock, and also determine the imbibition rate in pores of different sizes. The water saturation profiles obtained from the new model are validated against the waterflooding simulation results from the CMG, while the imbibition rates calculated by the model are validated against the experimental observations of gas–liquid spontaneous imbibition. The good match above indicates the newly proposed model can show the water saturation profile at a macroscopic scale while capture the underlying physics of the multiphase flow in a porous medium at a microscopic scale. Simulation results obtained from this model indicate that both wettability and viscosity ratio can affect the sequence of fluid imbibition into pores of different sizes during the multiphase flow, where less-viscous wetting fluid is preferentially imbibed into larger pores while more-viscous wetting fluid tends to be imbibed into smaller pores. Furthermore, this model provides an avenue to calculate the imbibition rate in pores of different sizes during wettability alteration and capture the non-Darcy effect in micro- and nano-scale pores.

© 2024 The Authors. Publishing services by Elsevier B.V. on behalf of KeAi Communications Co. Ltd. This is an open access article under the CC BY-NC-ND license (http://creativecommons.org/licenses/by-nc-nd/4.0/).

1. Introduction

Imbibition has a significant impact on the oil recovery rate in tight reservoirs (Gu et al., 2017; Meng et al., 2018; Yang et al., 2019; Guo et al., 2020). To gain a clear understanding of the imbibition mechanism, extensive research has been conducted on the imbibition behavior during the multiphase flow in porous media (Chen et al., 2020; Hussain et al., 2021; Lei et al., 2023; Nemer et al., 2020; Pak et al., 2023; Wu et al., 2020). To facilitate the study of the effects of interfacial tension, viscosity, and other factors on the imbibition behavior of different pores in porous media, researchers have modeled natural porous media (such as rock (Chen et al., 2012; Matthews et al., 2006; Zhou et al., 2013) and soil (Zhang et al., 2022)) and artificial porous media (such as microfluidic chips (Carrell et al., 2019; Gharibshahi et al., 2020; Lee et al., 2019; Liu et al., 2019; Rich et al., 2019)) as capillary bundle models consisting of capillary tubes with varying diameters. Numerous studies of imbibition behavior in single capillaries provide a foundation for exploring the physical mechanisms of multiphase flow in porous media. Washburn (1921) conducted a study on spontaneous imbibition of liquid-displacing-gas in a circular capillary tube. They found that the imbibition distance was proportional to the square

root of time, and this relationship became known as the Washburn equation. The Washburn equation quantitatively characterizes the effect of viscosity, contact angle, and capillary diameter on the imbibition rate during the imbibition process, as shown in Eq. (1):

$$l = \sqrt{\frac{r\sigma\cos\theta}{2\mu}t} \tag{1}$$

where r represents the radius of capillary tube, σ represents the surface tension, θ represents the contact angle, μ represents the dynamic viscosity of the fluid, and l represents the imbibition distance. In Washburn's spontaneous imbibition experiments, the displaced phase was gas, and thus the viscosity of the displaced phase was ignored in the establishment of Eq. (1). Mason and Morrow (2013) derived the complete form of Eq. (1) by taking into account the extra applied pressure drop and the viscosities of both the displacing and displaced phases, as shown in Eq. (2):

$$\frac{r^2}{8}\left(P_{\text{applied}} + P_{\text{c}}\right) \cdot t = \frac{1}{2}\left(\mu_1 - \mu_2\right) \cdot L^2 + \mu_2 \cdot L_{\text{tube}} \cdot L \tag{2}$$

where P_{applied} represents the extra applied pressure drop, P_{c} represents the capillary force, L_{tube} represents the length of a capillary tube, μ_1 and μ_2 represent the viscosities of the displacing and displaced phases respectively. Combined with Eq. (2), Mason and Morrow (2013) calculated the imbibition rate by adjusting the viscosity ratio. The results showed that the imbibition rate decreases with time as $\mu_1/\mu_2 > 1$, and increases with time as $\mu_1/\mu_2 < 1$.

Based on the understanding of imbibition behavior in single capillaries, researchers have established various mathematical models on the basis of a capillary bundle model to characterize multiphase flow in porous media. Some researchers used capillary bundle models without lateral interconnections among tubes to simulate the imbibition behavior of multiphase flow in porous media (Dahle et al., 2005; Xiong et al., 2017; Yang et al., 2009). Dahle et al. (2005) utilized a capillary bundle model composed of capillary tubes with varying diameters to model porous media and investigated the change of the imbibition distance with time in each tube. Xiong et al. (2017) applied this capillary bundle model to study the impact of the boundary layer on multiphase flow in tight reservoirs. Zhao et al. (2020) established a mathematical model based on the Poiseuille equation to characterize the imbibition behavior in a capillary bundle, considering the influence of the boundary layer and Bingham fluid flow, and analyzed the nonlinear imbibition phenomenon in tight reservoirs. Although the mathematical models based on the capillary bundle model without the cross-flow established by Xiong et al. (2017) and Zhao et al. (2020) can describe the phenomenon of imbibition in tight reservoirs, they have several limitations. This type of capillary bundle model assumes that each capillary tube is independent, resulting in simulation results that consistently show the leading front (referring to the front of the tube in the capillary bundle that has the longest imbibition distance) located in the largest capillary tube, which is inconsistent with the experimental results observed in spontaneous imbibition experiments where the leading front is located in the pores with the smallest pore size (Ashraf et al., 2017). Moreover, since the position of the leading front cannot be predicted, such models may have difficulties to accurately predict the shape of the displacement front and the distribution of the residual oil during the multiphase flow in porous media. Due to the fact that existing non-interacting capillary bundle models do not consider cross-flow among tubes, they fail to capture the physical mechanisms during the imbibition process within porous media, and consequently, they are incapable of describing the imbibition behavior within porous media.

Other researchers have considered the characteristics of connections among pores in tight reservoirs when establishing capillary bundle models. Dong et al. (1998) first proposed the concept of the interacting capillary bundle model (ICB model), in which different capillary tubes were connected with each other to allow cross-flow of fluids between capillary tubes. Subsequently, Dong et al. (2005) established a mathematical model based on the Poiseuille equation to characterize the imbibition behavior inside the ICB, and calculated the imbibition rate of the displacing phase and the position of the two-phase interface in different capillary tubes during the imbibition process. The results showed that the invasion of the displacing phase started from the capillary tube with the smallest diameter; during the imbibition process, the invading depth of the displacing phase was greater in capillary tubes with smaller diameters; in addition, the two-phase profile became steeper with the increasing displacement rate. Dong et al. (2006) used their mathematical model to simulate the process of waterflooding and analyzed the impacts of the length of the capillary bundle as well as the viscosity ratio of oil and water on oil recovery. Dong's mathematical model assumed pressure balance between different capillary tubes at any position along the direction of the capillary bundle in the single-phase region (Dong et al., 2005). Wang et al. (2008) suggested that the pressure needs to be balanced at the same locations of capillary tubes with the cross-flow. While the pressure between different capillary tubes tended to become balanced during the imbibition process, complete pressure balance could not be achieved. Wang and Dong (2011) developed an interacting triangular capillary bundle model using capillaries of equilateral triangle cross sections. The model simulated the trapping phenomenon of the crude oil (the non-wetting phase) in tight reservoirs during the imbibition process, and investigated the impacts of the oil−water viscosity ratio and capillary size distribution on the residual oil saturation. The results indicated that the larger the oil−water viscosity ratio, the higher the residual oil saturation. Furthermore, a more concentrated distribution of capillary sizes led to a lower residual oil saturation. Li et al. (2017) proposed a fully implicit solution method to calculate the interface positions at different times in the capillary tubes of an ICB model under eight different water-displacing-oil scenarios. The results indicated that the distances between interfaces became smaller when IFT was lowered. Ashraf et al. (2023) proposed a planar ICB model to predict the spontaneous imbibition behavior in a quasi-two-dimensional porous medium and investigated the influence of the arrangement order of capillary tubes on the imbibition length of the displacing phase inside tubes.

These mathematical models, established based on different ICB models, have demonstrated good predictive capabilities for the spontaneous imbibition behavior of gas−liquid in porous media (Bico and Quéré, 2003; Sun et al., 2016; Unsal et al., 2007). Unsal et al. (2007), Sun et al. (2016), Bico and Quéré (2003), Ashraf et al. (2017), and Lai et al. (2016) have all observed that the leading front during experiments of gas−liquid spontaneous imbibition in porous media is located in the smallest pores. Furthermore, Sun et al. (2016) observed in their experiment that as spontaneous imbibition progressed, the gap between the interfaces in small and large diameter capillary tubes increased; in the experiment conducted by Ashraf et al. (2017), it was observed that the arrangement order of capillary tubes with different diameters had a certain influence on the relative positions of the interfaces. In summary, it has been observed in experiments of spontaneous imbibition of gas−liquid in porous media that the imbibition distance in pores or capillary tubes with smaller diameters is greater than that in larger pores or capillary tubes. This observation is consistent with the prediction results of mathematical models based on ICBs.

Existing ICB models assume that the position of the

displacement front in pores of different sizes is primarily governed by the capillary force, with smaller pores exhibiting stronger capillary forces. As a result, imbibition initially occurs in the smallest pores, and the position of the displacement front within smaller pores is more forward (Dong et al., 1998). This premise may constrain the capability of ICB models in describing the imbibition behavior of oil–water in tight reservoirs, and may not reflect real physical phenomena during the imbibition process. For instance, it is commonly observed in coreflood experiments of water-wet tight rock that the recovered oil is mainly from the larger pores (Gao et al., 2021; Hou and Sheng, 2022; Liang et al., 2017). Additionally, results contradictory to the models have been observed in microfluidic experiments of water-displacing-oil and oil-displacing-water. Gaol et al. (2020) conducted experiments of water-displacing-oil and oil-displacing-water in a water-wet micromodel with two different permeable zones. The viscosity of water was 1.10 mPa s and that of oil was 13.82 mPa s. The results of water-displacing-oil experiments showed that the imbibition rate was faster in the high-permeability zone than in the low-permeability zone, and the leading front was located in the high-permeability zone. Similarly, the results of oil-displacing-water experiments showed that the leading front was also located in the high-permeability zone. Wolf et al. (2022) observed in oil-displacing-water experiments conducted on a water-wet microfluidic chip with dual porosity that the displacing phase mainly invaded tubes with larger pore sizes. In Wolf's experiments, the viscosity of oil (1.30 mPa s) was higher than that of water (0.89 mPa s). Observations from oil–water displacement experiments in tight rocks and microfluidic chips, contrary to the predictions of existing mathematical models of different ICBs, suggest that the influence of viscosity ratio and wettability on the leading front and the shape of displacement front may have been overlooked.

The current ICB models have successfully simulated the position of the leading front and the residual oil distribution in porous media, compared to non-interacting capillary models. However, their prediction on imbibition rates under varying conditions of wettability and viscosity ratios appears to be limited. Additionally, these ICB models fail to capture the underlying physics of capillary imbibition during wettability alteration induced by surfactants. Compared to existing ICB models, the mathematical model of the ICB developed in this paper not only accurately captures the physical phenomenon of cross-flow between pores during multiphase flow in porous media, but also considers the influence of viscosity ratio and wettability on imbibition behavior in different pores during multiphase flow. Furthermore, the model proposed in this paper unifies imbibition behavior within porous media under different wettability and viscosity ratio conditions. The model's simulation results align with experimental observations, encompassing spontaneous gas–liquid imbibition experiments and oil–water displacement experiments in tight rocks and microfluidic chips. Additionally, the effect of interfacial tension on oil recovery and the minimum pore size for oil flow is analyzed. The new mathematical model not only accurately reflects the position of the leading front and the shape of the displacement front during multiphase flow in porous media, but also provides a method to predict the distribution of the residual oil (in both large and small pores), the mobilization of crude oil, and the oil recovery during coreflood experiments in porous media.

2. Model description

2.1. Model formulation

The ICB model is used to reflect the pore characteristics of tight

rocks (Dong et al., 2005; Li et al., 2017). Currently, the simulation results of the ICB model can accurately predict the observation of a gas–liquid spontaneous imbibition experiment (Bico and Quéré, 2003; Sun et al., 2016; Unsal et al., 2007), but they do not yet capture the imbibition behavior in oil–water displacement experiments (Gao et al., 2021; Hou and Sheng, 2022; Liang et al., 2017). Therefore, analyzing imbibition behavior in tight rocks using the mathematical model of the ICB is a feasible approach. However, the current mathematical models have several limitations. Although the current mathematical models of different ICBs have considered the impact of viscosity on the shape of the displacement front during multiphase flow, the preset assumption (i.e., assuming the leading front is situated in the tube with the smallest diameter of the capillary bundle) seems to limit the accuracy of the models regarding multiphase flow behavior under different conditions in porous media. The position of the leading front is not predetermined in the process of establishing the mathematical model presented in this paper. Instead, the new model aims to accurately describe the multiphase flow behavior in natural or artificial porous media by capturing the existing physical phenomena.

Firstly, a capillary bundle model consisting of n capillary tubes with different diameters is constructed as shown in Fig. 1. The length of the capillary bundle is L, and the diameters of the tubes are arranged in the descending order from R_1 to R_n.

Each tube in this capillary bundle is initially saturated with either water, oil or gas. It is assumed that the left end of the capillary bundle model is connected to a container of displacing fluid. During the displacement, the displacing phase is injected from the left end while the displaced phase is pushed out from the right end. The interface positions in tubes 1 to n are denoted as x_1, $x_2, \ldots, x_m, \ldots, x_n$.

Subsequently, this paper establishes a new mathematical model
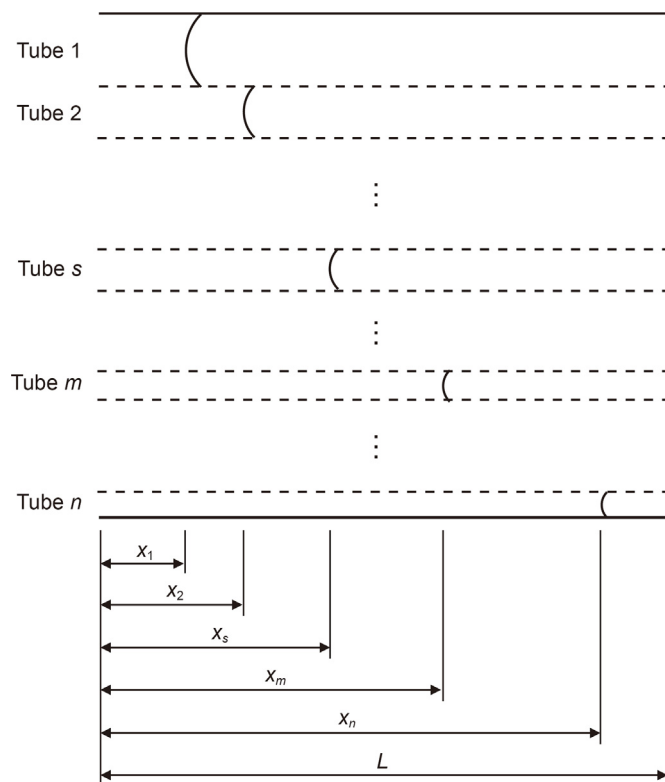

Fig. 1. Schematic diagram of the ICB model. The front (in tube n) corresponds to the leading front.

that describes the imbibition behavior in different capillary tubes of the ICB under the condition of constant pressure difference (ΔP). The driving force (ΔP_{total}) in any tube includes both capillary force (P_c) and an additional applied pressure drop (ΔP). For example, the driving force in tube m can be expressed as Eq. (3):

$$\Delta P_{\text{total}} = \Delta P + P_{cm} \tag{3}$$

where P_{cm} represents the capillary force in tube m.

It is believed that the imbibition behavior within each tube during the imbibition process satisfies the two-phase flow Poiseuille equation:

$$\Delta P + P_{cm} = \frac{8\mu_1 \cdot Q_m(t)}{\pi R_m^4} \cdot x_m + \frac{8\mu_2 \cdot Q_m(t)}{\pi R_m^4} \cdot (L - x_m) \tag{4}$$

In micro- to milli-scale channels, the non-Darcy effect is almost negligible, and Eq. (4) can calculate the imbibition rate with acceptable accuracy. However, in nano- to sub-micro-scale channels, the non-Darcy effect significantly influences the imbibition rate. Therefore, DLVO (Derjaguin, Landau, Verwey, and Overbeek) theory (Yuan et al., 2021; Zou et al., 2021) can be used to calculate the disjoining pressure and the liquid film thickness within the tubes, and make adjustments to the left-hand pressure term and the right-hand tube radius term in Eq. (4). In the micro- and nano-scale channels, the disjoining pressure becomes more significant and strongly affects the stability of the liquid film covering the solid surface, and further affects the liquid film thickness. During the imbibition process in micro- and nano-scale channels, the disjoining pressure and liquid film thickness influence imbibition behavior by constraining the volume available for liquid flow. Therefore, the disjoining pressure and liquid film thickness function as descriptors for nonlinear flow phenomena within micro- and nanoscale channels. The change of the imbibition distance within tube m with time can be derived from Eq. (4) and is expressed in Eq. (5):

$$\frac{r^2}{8}(\Delta P + P_{cm}) \cdot t = \frac{1}{2}(\mu_1 - \mu_2) \cdot x_m^2 + \mu_2 \cdot L \cdot x_m \tag{5}$$

Meanwhile, the imbibition behavior of the displacing phase and the displaced phase respectively conforms to the Poiseuille equation, as demonstrated by Eqs. (6) and (7),

$$P_{\text{in}} - P_{m1} = \frac{8\mu_1 \cdot Q_m(t)}{\pi R_m^4} \cdot x_m \tag{6}$$

$$P_{m2} - P_{\text{out}} = \frac{8\mu_2 \cdot Q_m(t)}{\pi R_m^4} \cdot (L - x_m) \tag{7}$$

P_{m1} and P_{m2} are subject to the following relationship:

$$P_{m2} = P_{m1} + P_{cm} \tag{8}$$

In the given equations, P_{m1} and P_{m2} respectively represent the pressures adjacent to the displacing phase and the displaced phase at the interface between the two phases; P_{in} and P_{out} represent the pressures at the inlet and outlet of the capillary bundle, respectively; μ_1 and μ_2 represent the viscosities of the displacing phase and the displaced phase, respectively; $Q_m(t)$ represents the volumetric flow rate within tube m at time t; R_m corresponds to the radius of tube m; x_m represents the imbibition distance within tube m.

After time t, under the condition of a constant pressure difference ($P_{\text{in}} - P_{\text{out}}$), the total volume of the displacing phase liquid flowing into the capillary bundle can be expressed as follows:

$$V_{\text{total}}(t) = \sum_{m=1}^{n} Q_m \cdot t = \sum_{m=1}^{n} \pi R_m^2 \cdot x_m \tag{9}$$

After the displacement phase invades capillary tubes with different diameters, the equilibrium of inter-tube pressure is disrupted, leading to the occurrence of pressure difference among tubes (in the regions of the displacing phase and the displaced phase). This pressure difference drives the cross-flow of fluids (including the displacing phase and the displaced phase) among tubes. Hence, at any given moment, cross-flow occurs among the tubes, and the pressures within different tubes maintains a dynamic equilibrium. For example, in the case of tube m, it exhibits cross-flow with the other $n-1$ tubes. The volumetric flow rates of cross-flow between tube m and the other tubes are denoted as $Q_{m(m\to1)}$, $Q_{m(m\to2)}$, …, $Q_{m(m\to m-1)}$, $Q_{m(m\to m+1)}$, …, $Q_{m(m\to n)}$, respectively. If $Q_{m(m\to s)}$ (indicating the cross-flow between tubes m and s) has a positive value, it signifies fluid flow from tube m to tube s. Conversely, if the value is negative, it indicates the fluid flows from tube s to tube m. The total volumetric flow rate of the cross-flow in tube m is expressed by Eq. (10):

$$Q_{m-\text{cross}} = \sum_{s=1}^{n} Q_{m(m\to s)} \ (s \neq m) \tag{10}$$

After considering the cross-flow, the volumetric flow rates within each tube can be expressed as follows:

$$Q_m^*(t) = Q_m(t) - Q_{m-\text{cross}}(t) \quad (Q_m^*(t) \geq 0) \tag{11}$$

After the occurrence of cross-flow among tubes, pressure equilibrium is restored among tubes, following Eqs. (12) and (13),

$$\text{Grad}(P_{m1}^*) = \text{Grad}(P_{s1}^*) \tag{12}$$

$$\text{Grad}(P_{m2}^*) = \text{Grad}(P_{s2}^*) \tag{13}$$

where $\text{Grad}(P_{s1}^*)$ and $\text{Grad}(P_{m1}^*)$ represent the pressure gradients within the displacing phase regions of tubes s and m, respectively, after pressure equilibrium among tubes is established. Similarly, $\text{Grad}(P_{s2}^*)$ and $\text{Grad}(P_{m2}^*)$ represent the pressure gradients within the displaced phase regions of tubes s and m, respectively, after pressure equilibrium among tubes is achieved.

$Q_m^*(t)$ is defined as the apparent volumetric flow rate, which represents the flow rate visually observed after the pressure equilibrium is achieved among tubes. On the other hand, $Q_m(t)$ is defined as the true volumetric flow rate, reflecting the actual flow entering the tube, encompassing both the apparent volumetric flow rate and the total cross-flow rate between the tubes. Moreover, x_m^* and x_m are defined as the apparent imbibition distance and the true imbibition distance, respectively.

At this time, the relationship among the apparent volumetric flow rate ($Q_m^*(t)$), the apparent imbibition distance (x_m^*), and pressure gradient (including $\text{Grad}(P_{m1}^*)$ and $\text{Grad}(P_{m2}^*)$) within each tube is governed by Eqs. (14) and (15):

$$\text{Grad}(P_{m1}^*) = \frac{P_{\text{in}} - P_{m1}^*}{x_m^*} = \frac{8\mu_1 \cdot Q_m^*(t)}{\pi R_m^4} \tag{14}$$

$$\text{Grad}(P_{m2}^*) = \frac{P_{m2}^* - P_{\text{out}}}{(L - x_m^*)} = \frac{8\mu_2 \cdot Q_m^*(t)}{\pi R_m^4} \tag{15}$$

Furthermore, the apparent volumetric flow rate and the imbibition distance also satisfy Eq. (4), as depicted in Eq. (16):

$$\Delta P + P_{cm} = \frac{8\mu_1 \cdot Q_m^*(t)}{\pi R_m^4} \cdot x_m^* + \frac{8\mu_2 \cdot Q_m^*(t)}{\pi R_m^4} \cdot \left(L - x_m^* \right) \tag{16}$$

After pressure equilibrium among tubes is established, the total volume (V_{total}^*) of the displacing phase liquid flowing into the capillary bundle can be expressed as follows:

$$V_{\text{total}}^*(t) = \sum_{m=1}^{n} Q_m^* \cdot t = \sum_{m=1}^{n} \pi R_m^2 \cdot x_m^* \tag{17}$$

By analyzing Eqs. (12)–(15), it can be inferred that when the pressure gradient within the displacing phase region in tube m is equivalent to the pressure gradient within the displacing phase region in tube s, the pressure gradients within the displaced phase region in both tubes are also equivalent.

After a time duration of t, the principle of mass conservation is satisfied in the inflow of the displacing phase into the capillary bundle both before and after cross-flow occurs, implying that the volume of the displacing phase entering the capillary bundle remains unchanged, regardless of considering or the cross-flow among tubes. This condition is described by Eq. (18):

$$V_{\text{total}}^*(t) = V_{\text{total}}(t) \tag{18}$$

In conclusion, for an ICB composed of n capillary tubes, the imbibition process considering the cross-flow and the corresponding equations can be summarized as follows.

(1) After pressure equilibrium among tubes is established, imbibition behavior occurs in each tube within a very short time interval. Under the condition of balanced pressure gradients, the imbibition behavior during this time interval satisfies the two-phase flow Poiseuille equation (Eq. (4)). After the occurrence of imbibition, the pressure equilibrium among tubes is disrupted, resulting in the generation of the pressure difference among tubes. The emergence of the pressure difference induces cross-flow of fluid between tubes, driving the restoration of the pressure equilibrium among tubes. After pressure equilibrium among tubes is achieved, the fluid flow within each capillary tube satisfies Eq. (16), with a total of n equations.

(2) Additionally, upon the restoration of the pressure equilibrium among tubes, the pressure gradients within the displacing phase (displaced phase) regions of any two tubes are equal, satisfying Eq. (12) (Eq. (13)), resulting in a total of $n-1$ equations.

(3) Before and after the pressure equilibrium (cross-flow) among tubes, the inflow of the displacing phase fluid into the capillary bundle obeys the law of mass conservation. In other words, the total volume of the displacing phase fluid entering the capillary bundle prior to equilibrium is equal to the total volume of the displacing phase fluid within the capillary bundle after equilibrium has been established (as indicated by Eq. (18)).

In the new mathematical model of the ICB, there are a total of $2n$ unknowns, comprising $Q_1^*(t)$ to $Q_n^*(t)$, x_1^* to x_n^*. Throughout the solution process, the nonlinear equations group comprises a total of $2n$ equations. With the $2n$ equations, the new mathematical model of the ICB can be solved. Furthermore, in the case where either the apparent volumetric flow rate ($Q_m^*(t)$) or the apparent imbibition distance (Q_m^*) within tube m is known, the other parameter can be determined by utilizing Eq. (16).

2.2. Solving procedure

To solve for the flow rate and interface position in each tube at different time points, we use Newton's iterative method for numerical solutions. The nonlinear equations group solved by the Newton iterative method consists of Eqs. (12), (16) and (18), and the process is as follows.

2.2.1. Newton's method for iterative solution

For any given time t, the flow rates and interface positions in each tube satisfy the above nonlinear equation system. The unknown variables are

$$[Y] = \left(x_1^*, x_2^*, \cdots, x_n^*, Q_1^*, Q_2^*, \cdots, Q_n^* \right)^{\mathrm{T}} \tag{19}$$

The residual form and iterative expressions of the Newton iteration equation group are constructed as shown in Eqs. (20) and (21):

$$\begin{cases} R_{m1} = \dfrac{8}{\pi R_m^4} Q_m^*(t) \left\{ \mu_1 x_m^*(t) + \mu_2 \left[L - x_m^*(t) \right] \right\} - \left(\Delta P + P_{cm} \right) \\ R_{m2} = \mathrm{Grad}\left(P_{m1}^* \right) - \mathrm{Grad}\left(P_{11}^* \right) \\ R_3 = V_{\text{total}}^*(t) - V_{\text{total}}(t) \end{cases} \tag{20}$$

$$[\bar{J}]\overline{\delta Y} = -\overline{R} \tag{21}$$

wherein,

$$\overline{R} = \left(R_{11}, R_{21}, \cdots, R_{n1}, R_{12}, R_{22}, \cdots, R_{(n-1)2}, R_3 \right)^{\mathrm{T}} \tag{22}$$

$$\overline{\delta Y} = \left(\delta x_1, \delta x_2, \cdots, \delta x_n, \delta Q_1, \delta Q_2, \cdots, \delta Q_n \right)^{\mathrm{T}} \tag{23}$$

$$[Y]^{i+1} = [Y]^i + [\overline{\delta Y}]^i \tag{24}$$

$$[\bar{J}] = \begin{pmatrix} \dfrac{\partial R_{11}}{\partial x_1} & \dfrac{\partial R_{11}}{\partial x_2} & \cdots & \dfrac{\partial R_{11}}{\partial x_n} & \dfrac{\partial R_{11}}{\partial Q_1} & \dfrac{\partial R_{11}}{\partial Q_2} & \cdots & \dfrac{\partial R_{11}}{\partial Q_n} \\ \dfrac{\partial R_{21}}{\partial x_1} & \dfrac{\partial R_{21}}{\partial x_2} & \cdots & \dfrac{\partial R_{21}}{\partial x_n} & \dfrac{\partial R_{21}}{\partial Q_1} & \dfrac{\partial R_{21}}{\partial Q_2} & \cdots & \dfrac{\partial R_{21}}{\partial Q_n} \\ \vdots & \vdots & & \vdots & \vdots & \vdots & & \vdots \\ \dfrac{\partial R_{n1}}{\partial x_1} & \dfrac{\partial R_{n1}}{\partial x_2} & \cdots & \dfrac{\partial R_{n1}}{\partial x_n} & \dfrac{\partial R_{n1}}{\partial Q_1} & \dfrac{\partial R_{n1}}{\partial Q_2} & \cdots & \dfrac{\partial R_{n1}}{\partial Q_n} \\ \dfrac{\partial R_{12}}{\partial x_1} & \dfrac{\partial R_{12}}{\partial x_2} & \cdots & \dfrac{\partial R_{12}}{\partial x_n} & \dfrac{\partial R_{12}}{\partial Q_1} & \dfrac{\partial R_{12}}{\partial Q_2} & \cdots & \dfrac{\partial R_{12}}{\partial Q_n} \\ \dfrac{\partial R_{22}}{\partial x_1} & \dfrac{\partial R_{22}}{\partial x_2} & \cdots & \dfrac{\partial R_{22}}{\partial x_n} & \dfrac{\partial R_{22}}{\partial Q_1} & \dfrac{\partial R_{22}}{\partial Q_2} & \cdots & \dfrac{\partial R_{22}}{\partial Q_n} \\ \vdots & \vdots & & \vdots & \vdots & \vdots & & \vdots \\ \dfrac{\partial R_{(n-1)2}}{\partial x_1} & \dfrac{\partial R_{(n-1)2}}{\partial x_2} & \cdots & \dfrac{\partial R_{(n-1)2}}{\partial x_n} & \dfrac{\partial R_{(n-1)2}}{\partial Q_1} & \dfrac{\partial R_{(n-1)2}}{\partial Q_2} & \cdots & \dfrac{\partial R_{(n-1)2}}{\partial Q_n} \\ \dfrac{\partial R_3}{\partial x_1} & \dfrac{\partial R_3}{\partial x_2} & \cdots & \dfrac{\partial R_3}{\partial x_n} & \dfrac{\partial R_3}{\partial Q_1} & \dfrac{\partial R_3}{\partial Q_2} & \cdots & \dfrac{\partial R_3}{\partial Q_n} \end{pmatrix} \tag{25}$$

2.2.2. Solution steps

To solve for the flow rates and interface positions at any time t, the time step is set to Δt, where $\Delta t = 0.01$ s. At the ith time step, the corresponding total time is $t = i \cdot \Delta t$.

The detailed solution steps are outlined as follows.

Step 1: When $i = 1$, with $t = \Delta t$, the true imbibition distance $x_m(\Delta t)$ is computed using Eq. (5). Subsequently, the true volumetric flow rate $Q_m(\Delta t)$ and the total volume of the displacing phase $V_{\text{total}}(\Delta t)$ entering the capillary bundle are calculated separately based on Eqs. (4) and (9) respectively. And then, arbitrary initial values of cross-flow rate between tubes are given

$$[Q_{\text{cross}}]^0 = \left(Q_{1-\text{cross}}^0, Q_{2-\text{cross}}^0, \cdots, Q_{n-\text{cross}}^0 \right)^{\text{T}} \tag{26}$$

Based on Eqs. (11), (16) and (26), the expressions for the apparent volumetric flow rate and the apparent imbibition distance can be derived. The matrix form is expressed as Eq. (27):

$$[Y]^0 = \left(x_1^{*0}, x_2^{*0}, \cdots, x_n^{*0}, Q_1^{*0}, Q_2^{*0}, \cdots, Q_n^{*0} \right)^{\text{T}} \tag{27}$$

wherein, the superscript "T" denotes the transpose of the matrix.

Step 2: Calculate $[\bar{J}]^0$ and $[\bar{R}]^0$ by using $[Y]^0$, and then compute $[\bar{\delta}Y]^0$ by combining Eq. (21);

Step 3: Substituting $[\bar{\delta}Y]^0$ into Eq. (24), $[Y]^1$ can be obtained, and then $[\bar{J}]^1$ and $[\bar{R}]^1$ can be derived by further calculation; subsequently, repeat step 2 to calculate $[\bar{\delta}Y]^1$;

Step 4: Check whether $[\bar{\delta}Y]^1$ is less than ε (precision requirement). If the precision requirement is met, stop the iteration; otherwise, repeat steps 2 and 3 to continue the iteration until $[\bar{\delta}Y]^1$ is less than ε;

Step 5: Repeat steps 1 to 4 to calculate the apparent volumetric flow rates ($Q_m^*(i \cdot \Delta t)$) and the apparent imbibition distances ($x_m^*(i \cdot \Delta t)$) in each tube at time $t = i \cdot \Delta t$.

3. Model validation

Using two case studies, this section validates the simulation performance of the new mathematical model in predicting the spontaneous imbibition behavior of gas–liquid in different tubes within porous media and the changes in water saturation during the displacement process in tight reservoirs.

3.1. Case 1: Spontaneous imbibition of liquid-displacing-air

In spontaneous imbibition experiments of ICBs, a common phenomenon is observed where the leading front is located inside the capillary tube with smallest diameter (Ashraf et al., 2017; Bico and Quéré, 2003; Sun et al., 2016). During the process of gas–liquid spontaneous imbibition, the forces involved are mainly the capillary force and the viscous forces of the displacing phase. In this section, the experimental data published by Unsal et al. (2007) is selected, and the new mathematical model is used to calculate the change of the imbibition distance with time in tubes with different diameters, under the experimental conditions.

3.1.1. Experimental data

In Unsal's paper, spontaneous imbibition experiments were conducted using an ICB composed of three capillary tubes. The invading fluid was liquid paraffin with a viscosity of 180 mPa s and a surface tension of 33.83 mN/m. Liquid paraffin was considered as a fully wetting oil phase, with an approximate contact angle of 0°. The experimental results demonstrated a linear relationship between the square root of the imbibition distance and time,

consistent with the predicted results of the Washburn equation (Washburn, 1921) for gas–liquid imbibition behavior. In this paper, the data of Unsal's co-current spontaneous imbibition process with a groove angle (referring to the angle between the flat glass plate and the groove) of 85° is selected for comparative analysis, as shown in Fig. 2. Here, d represents the gap between the circular rod and the upper surface, R represents the radius of the circular rod, c represents the width of the small tube, and β represents the angle between the upper glass plate and the groove.

Fig. 2(a) illustrates that the cross-sectional geometry of the three capillary tubes in Unsal's experimental capillary bundle model is irregular. When utilizing the new mathematical model to predict the imbibition behavior under experimental conditions, the diameters of the tubes represent the sole uncertain input parameter. Therefore, the hydraulic radii (Lala and El-sayed, 2015) of the three capillary tubes are calculated in this section. The formula for calculating the hydraulic radius is as follows:

$$R_{\text{h}} = \frac{A}{P} \tag{28}$$

where R_{h} represents the hydraulic radius; A represents the cross-sectional area of the tube completely wetted by the wetting phase; P represents the wetted perimeter of the cross-sectional area. As shown in Eq. (29), the radius of a circular capillary tube is twice the hydraulic radius of an irregular capillary.

$$R_{\text{h-circle}} = \frac{A}{P} = \frac{\pi R_{\text{circle}}^2}{2\pi R_{\text{circle}}} = \frac{R_{\text{circle}}}{2} \tag{29}$$

where $R_{\text{h-circle}}$ represents the hydraulic radius of an irregular capillary in Unsal's interacting capillary bundle; R_{circle} represents the radius of the circular capillary that is converted from the irregular one.

In this case, the radius of the circular rod (R) is 1.58 mm, the groove angle (β) is 85°, and the gap (d) between the glass plate and the rod is 0.2 mm. During the calculation of the hydraulic radius, the width of the small capillary (c) is given as 1.18 mm. The wetted perimeter (P) and cross-sectional area (A) of the large, medium, and small capillary tubes are then separately calculated. The hydraulic radii of the large, medium, and small capillary tubes in the experimental capillary bundle model are calculated using Eq. (28) and are found to be approximately 0.179, 0.130, and 0.117 mm, respectively.

3.1.2. Comparison of simulation and experimental results

An ICB model comprising three circular capillary tubes is designed, and the radii of the three tubes are determined to be 0.358, 0.260, and 0.234 mm, respectively, using Eq. (29) and the previously calculated hydraulic radii. The change of the imbibition distance with time for each tube in this ICB with three channels is calculated under given conditions of fluid viscosity, surface tension, and solid–liquid–gas contact angle. The experimental results are compared with the calculated results, as depicted in Fig. 3. The calculation results indicate that the leading front is located in the small pores when the more-viscous wetting fluid displaced air through spontaneous imbibition. The results calculated by the new mathematical model are consistent with the phenomenon observed in spontaneous imbibition experiments in porous media (Ashraf et al., 2017; Bico and Quéré, 2003; Sun et al., 2016). The comparison results show that the calculated results match well with the experimental results (Unsal et al., 2007) in terms of the change of imbibition distance with time for the small and medium tubes, with deviations of 2.31% and 2.32%, respectively. For the large tubes, a lower matching degree of 19.35% is observed.
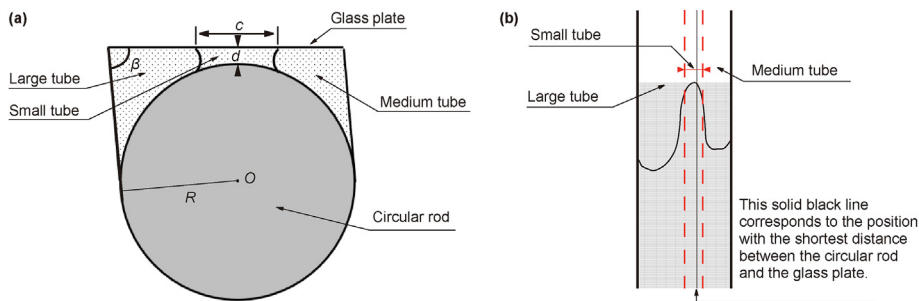
Fig. 2. Schematic of the cross-section (**a**) and longitudinal section (**b**) of the capillary bundle used in Unsal's spontaneous imbibition experiments (Unsal et al., 2007).
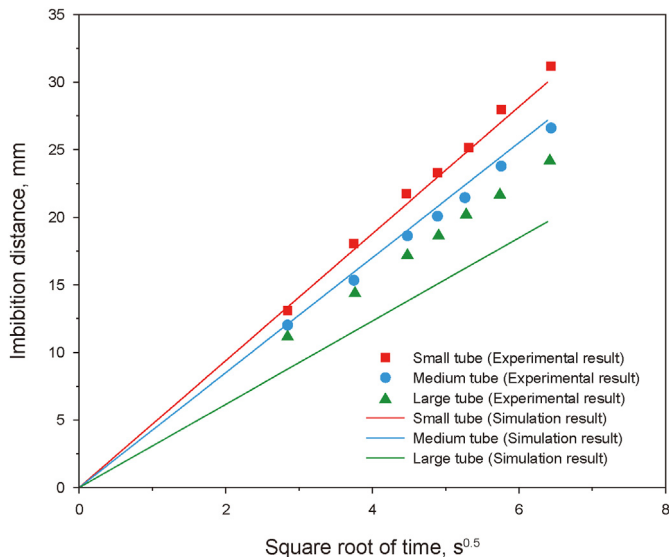

Fig. 3. Comparison of simulation and experimental results (Unsal et al., 2007).

As shown in Fig. 2(b), the shape of the displacement front in the three capillary tubes during the imbibition process deviates from that shown in Fig. 2(a), exhibiting a leftward tilt towards the large tube. Therefore, in the actual imbibition processes, the hydraulic radius of the large tube is smaller than the calculated value, and the actual values of the three hydraulic radii are closer. As a result, the actual imbibition rate (the change of imbibition distance with time) in the large tube is closer to those in the medium and small tubes compared to the simulation results.

In general, considering the irregular shape influence, the new mathematical model exhibits excellent predictive capability in estimating the imbibition rate of capillary tubes with different diameters during the spontaneous imbibition process in Unsal's ICB.

3.2. Case 2: Numerical simulation of water-displacing-oil

The ICB model has the ability to simulate the changes in water saturation during water imbibition in tight reservoirs (Dong et al., 2006). Therefore, in this section, a water-wet tight reservoir is established using numerical simulation software, and the new mathematical model is used to predict the changes in water saturation curve over time at different locations after determining various parameters. In addition, the calculation results show that the leading front is located in the tube with the largest diameter during the displacement process of water-displacing-oil.

3.2.1. Numerical model of the reservoir

The 2D plan view of the geological reservoir established using CMG numerical simulation software is shown in Fig. 4. The reservoir is water-wet with a length of 18 m, porosity of 8.5%, and permeability of 0.3 mD. The original formation pressure is 20 MPa, and the bound water saturation is set to 28%. The reservoir contains two parallel fractures of equal length, and a well is placed in the middle of each fracture. The injection well is located on the left, and the production well on the right. The permeability of the fractures is set to 1000 mD, which is much larger than that of the matrix reservoir, ensuring that the injected water enters the fractures before entering the matrix. The high permeability of the fractures reduces the pressure drop within the fractures, ensuring that the pressure remains constant at all locations within the fractures. During the waterflooding simulation process, the viscosity of water is set to 1.0 mPa s, the viscosity of oil is set to 1.2 mPa s. The water saturation curves are recorded for three different pressure differentials, namely 10, 15, and 20 MPa.

In conventional coreflood experiments, permeability is used to characterize the ability of porous media to allow fluid flow. The larger the permeability, the greater the fluid ability to pass through. Li et al. (2023) and Zhao et al. (2022) investigated the change of rock permeability with its average pore radius. The results showed that there is a positive correlation between rock permeability and average pore radius, as shown in Fig. 5. The good correlation once again confirms that the ICB model can be used to characterize the imbibition behavior in different pores within porous media.

3.2.2. Determination of the radius range and volume distribution of capillary tubes

To predict the saturation changes during oil–water displacement process in porous media using the new mathematical model, the model parameters should not only specify the contact angle, interfacial tension, and viscosities of oil and water, but also the radius range of capillary tubes, as well as the volume distribution of
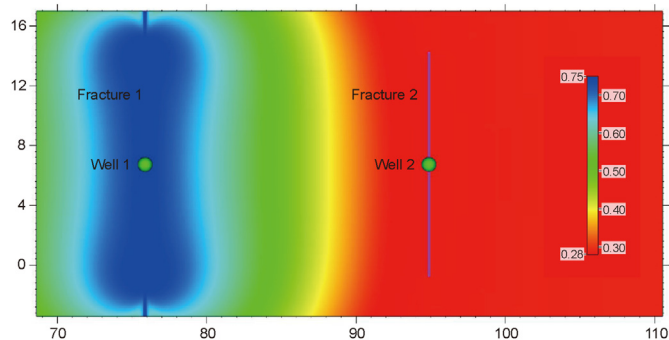

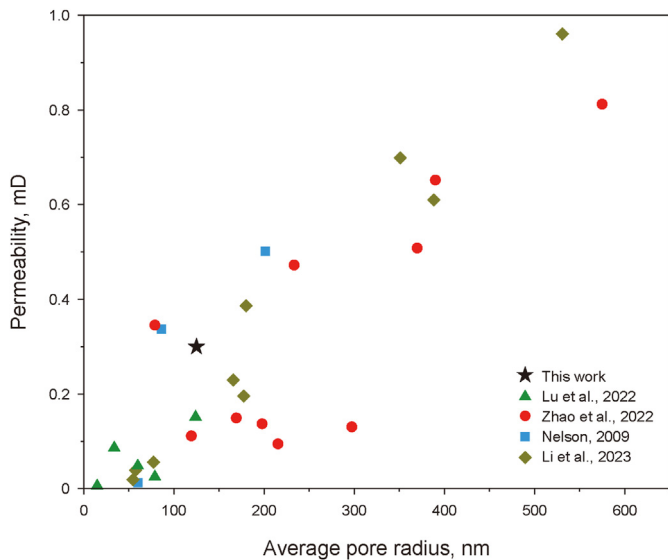**Fig. 4.** The plan view of the geological model.

Fig. 5. Correlation between permeability and average pore radius. The blue square data points are from Nelson (2009), the green triangular data points are from Lu et al. (2022), the red circular data points are from Zhao et al. (2022), and the dark yellow diamond data points are from Li et al. (2023). In addition, the black pentagram represents the permeability in our numerical model and the average pore radius in the mathematical model.

capillary tubes.

Firstly, by adjusting the radius range and the volume distribution of capillary tubes, the water saturation curve is computed using the new mathematical model. Subsequently, the radius distribution of capillary tubes are determined by fitting the numerical simulation results (the water saturation curve) under a pressure difference of 10 MPa. The radius distribution is shown in Fig. 6 where, the water saturation curve of the ICB model exhibits a good match to that of the homogeneous reservoir, as illustrated in Fig. 7(a) in Section 3.2.3. Then, the saturation distribution is calculated for pressure drops of 15 and 20 MPa using the radius distribution and the newly proposed mathematical model.

Qin et al. (2022) and Gostick (2017) proposed that the radius distribution of pores in homogeneous rocks typically exhibits a
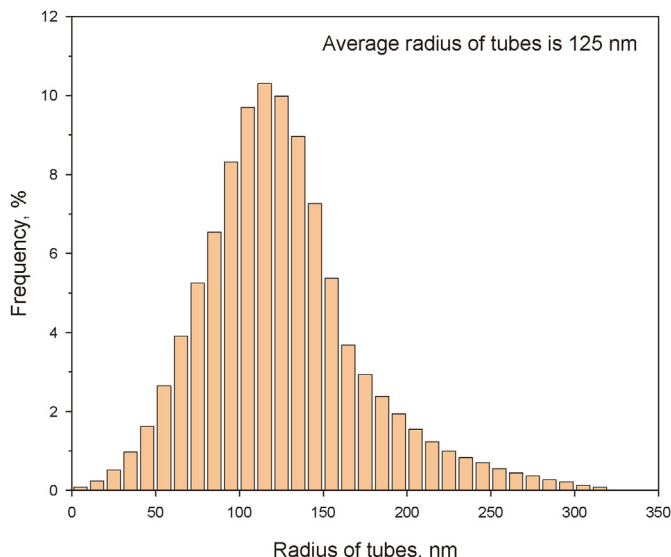

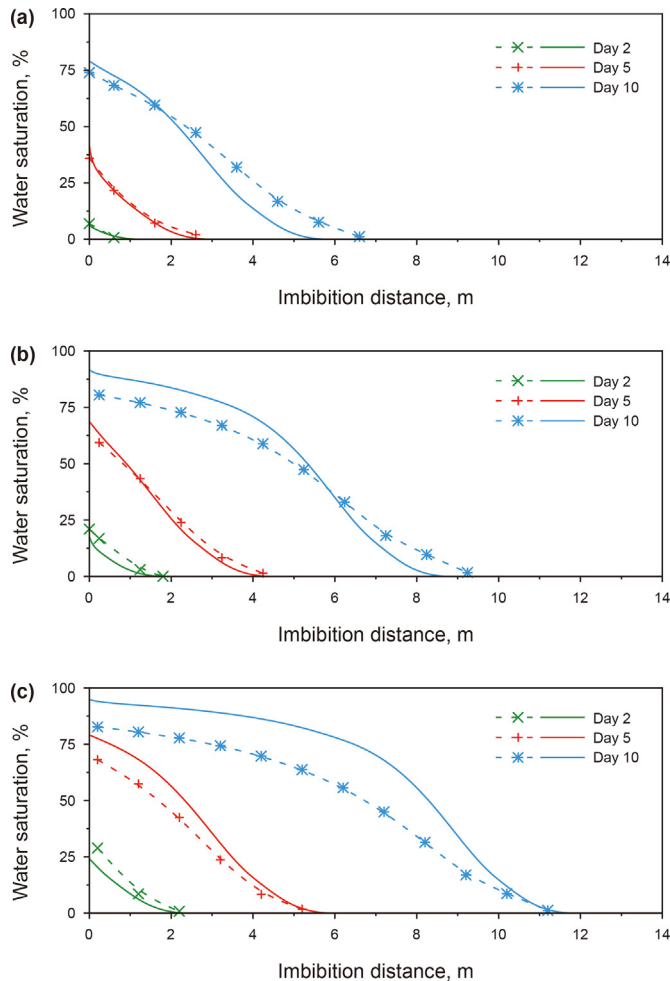**Fig. 6.** Diagram of the radius distribution of capillary tubes.

Fig. 7. Comparison of water saturation curves. The displacement pressure drops are 10 (**a**), 15 (**b**), and 20 MPa (**c**), respectively. The dashed lines represent the simulation results from CMG, and the solid lines represent the simulation results from the new mathematical model.

positively skew distribution, which is applied in the following calculation of this study.

3.2.3. Prediction and comparison

The waterflooding process in this tight reservoir is stimulated using the numerical model with adjusted displacement pressure drops of 15 and 20 MPa, and we record the water saturation curves at different times, as shown by the dashed lines in Fig. 7(b) and (c). Using the new mathematical model, the distributions of the displacement front in capillary tubes of different radii under the displacement pressure drops of 15 and 20 MPa are calculated. By combining the radius distribution of capillary tubes shown in Fig. 6, the water saturation curves are obtained, as shown by the solid lines in Fig. 7(b) and (c). Fig. 7(b) and (c) shows a high level of agreement between the water saturation curves obtained by the two methods. The results indicate that, under the conditions of known viscosity, interfacial tension, radius range, and volume distribution of capillary tubes, the new mathematical model of the ICB established in this study can predict the imbibition behavior in natural tight reservoirs and exhibits good predictive accuracy.

Subsequently, the average pore radius of the capillary bundle model shown in Fig. 6 is calculated to be 125 nm. The average pore radius (125 nm) of the capillary bundle model corresponds to a

permeability of 0.3 mD in the numerical model, as shown by the black pentagram in Fig. 5. The position of the black pentagram in Fig. 5 conforms to the overall trend between the average pore radius and permeability. This suggests that the new mathematical model can predict the imbibition behavior in porous media during the waterflooding process effectively. In addition, the good predictive performance indicates that the mathematical model can reflect the shape of displacement front and water saturation profile at any time at the reservoir scale, providing a new research tool for the imbibition behavior during the waterflooding process in reservoirs.

Furthermore, this model offers the potential to incorporate the solid-liquid interfacial interactions, such as disjoining pressure and liquid film thickness, for characterizing nonlinear flow phenomena within micro- and nano-scale pores.

In this section, the new mathematical model is used to match the gas−liquid imbibition behavior in the ICB model and predict the water saturation curves during the waterflooding process under a constant displacement pressure drop in tight reservoir. Both cases demonstrate good prediction results. According to the computational results of the mathematical model, the leading front during the gas−liquid imbibition process is located in the capillary tube with the smallest diameter. In contrast, during the process of less-viscous wetting phase (water) displacing the more-viscous non-wetting phase (oil), the leading front is located in the capillary tube with the largest diameter, consistent with the experimental observation (Gaol et al., 2020; Wolf et al., 2022). The two cases not only demonstrate the significant influence of viscosity ratio and wettability on the imbibition behavior during the displacement process in porous media, but also illustrate that the new model is capable of capturing the effects of wettability and viscosity ratio on the sequence of fluid entry and the shape of displacement front during the imbibition process in tight reservoirs.

4. Model application

This section employs the new mathematical model to compute the relative position of the interface in distinct tubes of the capillary bundle under different conditions of wettability and viscosity ratio to qualitatively analyze the position of the leading front and the shape of the displacement front during the imbibition process under different oil−water viscosity ratios in water-wet and oil-wet reservoirs. The effects of interfacial tension and viscosity on the minimum pore size for oil flow, water saturation profile, and oil recovery during displacement process in porous media are analyzed. Furthermore, the potential applications of the new mathematical model in the displacement process in tight reservoirs are discussed.

4.1. Effect of viscosity ratio and wettability on the leading front

Currently, various imbibition experiments in porous media have been conducted, including coreflood experiments for oil recovery and microfluidic chip experiments for oil displacement. Research results have shown that the difference in wettability and viscosity ratio can affect the leading front and the order of fluid entry into large and small pores during the imbibition process (Gaol et al., 2020; Unsal et al., 2007; Wolf et al., 2022). In the process of establishing the mathematical model of the ICB, the significant influence of viscosity ratio and wettability does not seem to have been recognized. The new mathematical model established in this paper based on the ICB considers the combined effects of wettability and viscosity ratio on the sequence of fluid invasion during the displacement process in porous media.

The computational results in the model validation section

demonstrate that, when a more-viscous wetting fluid is used as the displacing phase, the front of the invading fluid enters the capillary tubes with the smallest diameter first. Conversely, when a less-viscous wetting fluid is used as the displacing phase, the front of the invading fluid enters the capillary tubes with the largest diameter first. However, all parameters, such as fluid properties and pore size distribution, of the ICB model are different for the two cases discussed in the model validation section. To facilitate the comparison of the shape of displacement front under different conditions of viscosity ratio and wettability, a 5 cm long ICB model consisting of 32 tubes is designed in this section. The radii of tubes are uniformly distributed from $R_{min} = 50$ nm to $R_{max} = 100$ nm. The variation of the imbibition distance with time in capillary tubes of different diameters is calculated using a mathematical model for four combinations of wettability and viscosity ratio. The interfacial tension is set at 30 mN/m, and the viscosities of the less-viscous and more-viscous fluids are set at 1 and 9 mPa s, respectively. For the case of the wetting phase as the displacing fluid, the contact angle is set to 7.5° and the displacement pressure difference is set to 0.5 MPa. Conversely, for the non-wetting phase as the displacing fluid, the contact angle is set to 172.5°, and the displacement pressure difference is set to 1.7 MPa to overcome the capillary force and ensure that all tubes are invaded during the displacement process.

The calculation results are shown in Fig. 8. Fig. 8(a) and (d) clearly illustrate that, in the case of the less-viscous wetting fluid and more-viscous non-wetting fluid as the displacing phases, the leading front is located in the capillary tube with the largest diameter, and as imbibition proceeds, the displacing phase progressively invades tubes with decreasing diameter. Conversely, in the other two scenarios depicted in Fig. 8(b) and (c), the leading front is situated in the capillary tube with the smallest diameter. As the imbibition proceeds, the displacing phase is gradually drawn into tubes with increasing diameters.

In the new mathematical model of the ICB established in this paper, interfacial tension, contact angle, viscosity (including that of both the displacing and displaced phases) are all input parameters. The impact of viscosity ratio and wettability on the leading front is explained through the following case. As depicted in Fig. 9, the imbibition process divides the capillary bundle into three zones, comprising two single-phase regions (illustrated by blue and red zones in Fig. 9) and one two-phase region (shown by the orange zone in Fig. 9). The diameter of Tube 1 is smaller than that of Tube 2. Within the single-phase region, there is no pressure difference between two tubes at the same location along the direction of the ICB. In the case where less-viscous wetting fluid is used as the displacing phase, the leading front is located in the capillary tube with the largest diameter. In this scenario, the pressure gradient in the displacing phase region is smaller than that in the displaced phase region, as shown in Fig. 9(c). In the two-phase region, Tube 1 is filled with the displaced phase while Tube 2 is filled with the displacing phase. Therefore, the pressure gradient inside Tube 1 and Tube 2 respectively matches that of the displaced phase and the displacing phase region. As shown in Fig. 9(c), two vertical lines represent the capillary forces inside Tube 1 and Tube 2, P_{c1} and P_{c2}, respectively. P_{c1} is significantly larger than P_{c2}, which is consistent with the fact that Tube 1 has a smaller diameter than Tube 2 in Fig. 9(a). Similarly, the position of the leading front can be analyzed for the other three cases by considering Fig. 9(d), (e), (f).

The new mathematical model elucidates the influence of wettability and viscosity ratio on the location of the leading front and the shape of displacement front. This provides a qualitative method for analyzing the invasion position of the displacing phase in pores of different sizes during multiphase flow in tight rocks. Additionally, by integrating analysis of nuclear magnetic resonance
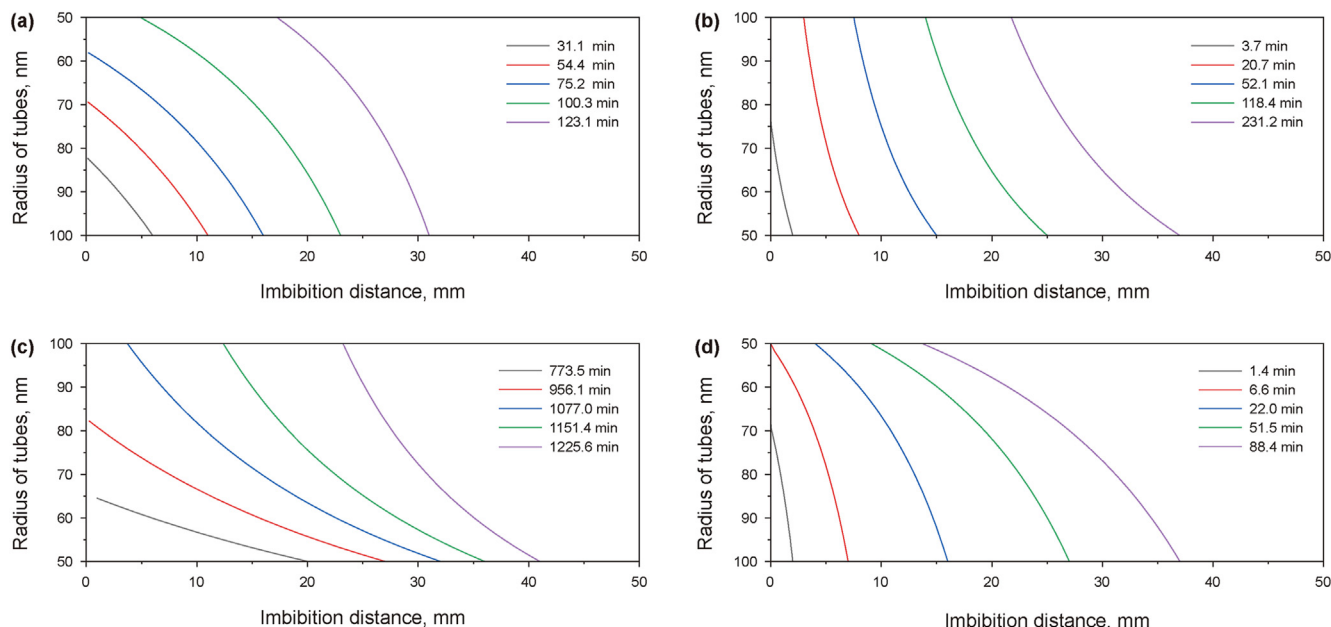
Fig. 8. The shape of the displacement front in the ICB with tubes of different radii. The less-viscous wetting fluid (**a**), more-viscous wetting fluid (**b**), less-viscous non-wetting fluid (**c**), and more-viscous non-wetting fluid (**d**) are as displacing phase, respectively.

(NMR) T_2 spectra and mercury intrusion porosimetry (MIP), it is anticipated that the displacement front position and distribution within different pores can be quantified during coreflood experiments in tight rocks.

4.2. Effect of interfacial tension on the minimum pore size for oil flow

During the process of stimulation in tight reservoirs, surfactants (wettability modifiers) are commonly added to fracturing fluids to enhance oil recovery (Yan et al., 2023; Zhao et al., 2022). For water-wet reservoirs, the addition of surfactants can increase the capillary number, thereby enhancing oil recovery (Johannessen and Spildo, 2013). In addition, reducing interfacial tension significantly reduces the capillary force, thereby greatly increasing the recovery of fracturing fluid during the backflow period, which is beneficial for enhancing oil recovery (Wijaya and Sheng, 2020). For oil-wet reservoirs, surfactants can alter the wettability of the reservoirs, thereby improving the efficiency of oil production through spontaneous imbibition (Kathel and Mohanty, 2013). Currently, NMR technology has been applied to coreflood experiments, where the relaxation time in the NMR T_2 spectrum can be correlated with the pore size distribution of tight rock cores, enabling the differentiation of various pore sizes. Researchers employ NMR technology to measure the hydrogen signals in pores of different sizes during coreflood experiments at different time intervals, thereby monitoring the oil saturation in different pores (Adenutsi et al., 2019; Lyu et al., 2018, 2020). Combining T_2 spectrum analysis, researchers can investigate the impact of factors such as interfacial tension on the oil recovery within individual pore sizes.

Fortunately, the new mathematical model has the potential to predict the recovery rate in pores of different sizes and the overall recovery rate under given conditions of interfacial tension, viscosity, and other factors in coreflood experiments. This section employs the new mathematical model to analyze the influence of interfacial tension on oil recovery and the minimum size of mobilizable oil within porous media during the displacement processes. The ICB model used in this section is the same as that in Section 4.1.

The frequency of radius distribution for the capillary bundle model is designed as illustrated in Fig. 11. The viscosities of water and oil are set as 1 and 9 mPa s, respectively. As depicted in Fig. 10, the ICB model is initially saturated with oil in each tube, represented by the orange solid line. The area enclosed by the curves and the horizontal axis represents the volume of the oil phase.

Fig. 10 illustrates the residual oil volume within each tube and the corresponding EOR under varying interfacial tension conditions when the leading front reaches the same position (approximately 6/10 of the total length of the capillary bundle). The results demonstrate that as the interfacial tension decreases from 2 to 0.6 mN/m, EOR increases from 5.53% to 25.48%, and the minimum pore radius for oil flow reduces from 85.5 to 61.3 nm. In conclusion, the new mathematical model clarifies the limiting radius for oil flow under different conditions, providing a new approach for determining the residual oil saturation and enhancing the residual oil recovery.

The new mathematical model is expected to explore the underlying physical mechanisms of immiscible displacement processes in pores of tight rocks through the synergy of nuclear magnetic resonance and microfluidic technologies. Unconventional oil and gas reservoirs, including tight oil, tight gas, shale oil, and shale gas, are primarily characterized by the presence of micro-to nano-scale pores in the rock matrix, which exhibit complex non-linear flow behavior inside (Zou et al., 2012). In the flow process within micro-nano confined spaces, the liquid film on the pore wall has significant different characteristics from bulk fluids (Thompson, 2018). At the micro- and nano-scale, intermolecular forces between reservoir fluids and the rock surface can affect their properties (like the density, surface tension, and the affinity), which then affects the imbibition process (Zou et al., 2021). Kelly et al. (2018) conducted experiments of polar and nonpolar fluids displacing gas on a nano-scale microfluidic chip. The results showed that the measured imbibition rate differs greatly from the predicted imbibition rate using the classical Washburn equation. The significant deviation between the measured imbibition rate and the predictions of traditional models in micro- and nano-scale porous media implies that scientists should question the predictive ability of traditional
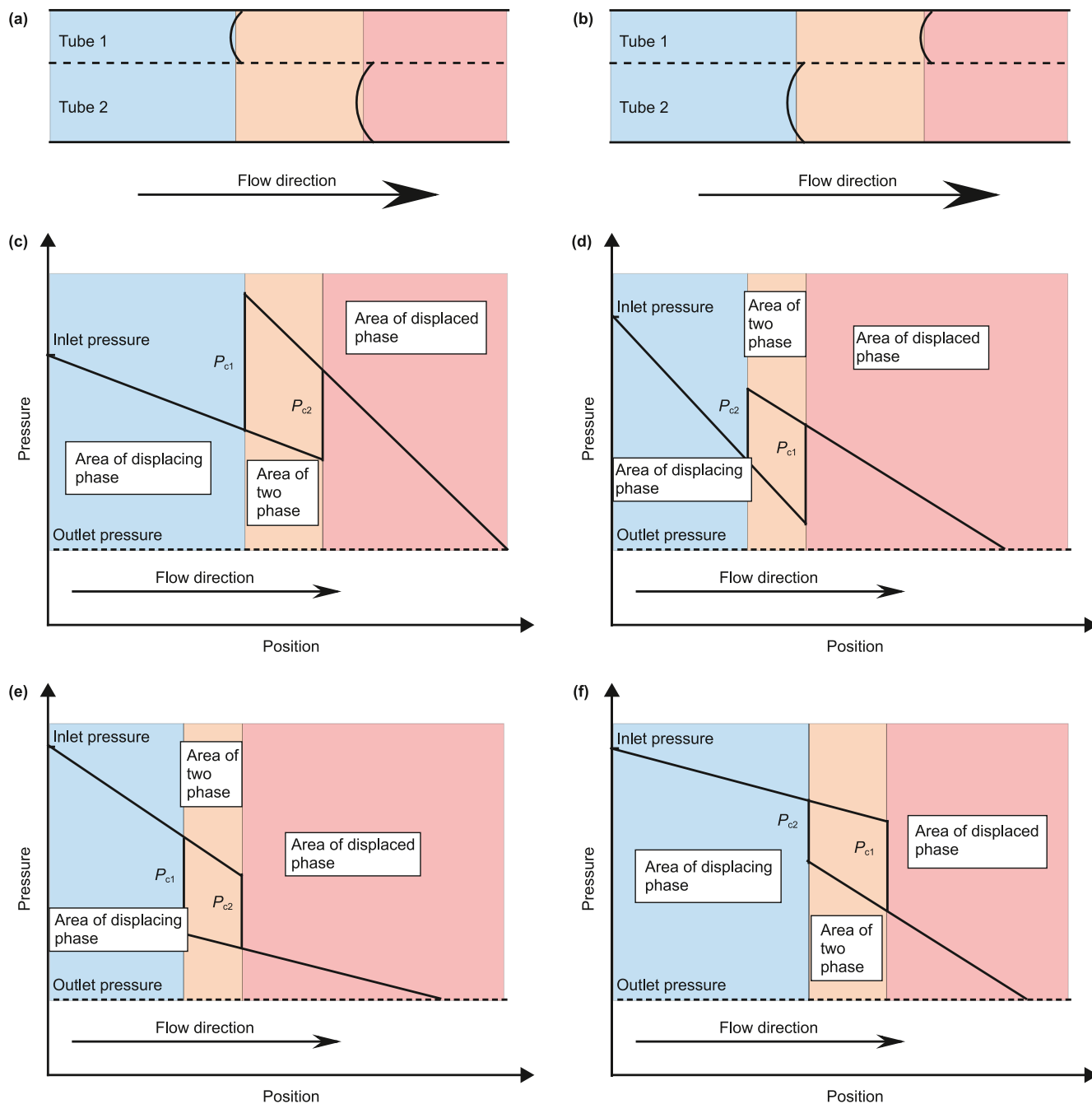
Fig. 9. Pressure gradient diagram in the dual-tube ICB.

models and investigate the effect of pore scale on fluid properties such as viscosity and interfacial tension in the nano-scale confinement. The new mathematical model not only offers a fundamental framework for modifying the imbibition model to predict fluid behavior in micro- and nano-scale porous media but also provides an expanded framework for introducing the effects of polar fluid adsorption-induced pore space reduction, dynamic contact angle changes.

Additionally, by combining the effects of wettability and viscosity ratio on the displacement front profile and the leading front, the distribution of water and oil within pores of different sizes in unconventional reservoirs during diverse production operations can be qualitatively evaluated. The fluid flow behavior of oil-wet

reservoirs during the process from hydraulic fracturing to production can be analyzed as an example. During the hydraulic fracturing and shut-in stages, the bottom-hole pressure is greater than the reservoir pressure. As a result, the water-based fracturing fluid, which is a non-wetting phase fluid, invades the pores and the leading front is located in the smallest pores, as shown in Fig. 8(c). After a prolonged exposure to water-based fluids containing wetting reversal agents, the reservoir undergoes a wettability alteration towards a water-wet state. During the subsequent flowback and production stages, the bottom-hole pressure decreases and the oil in the reservoir flows into the bottom of the well due to the pressure difference and oil swelling. At these stages, the oil is a non-wetting phase fluid and the leading front is located in the larger
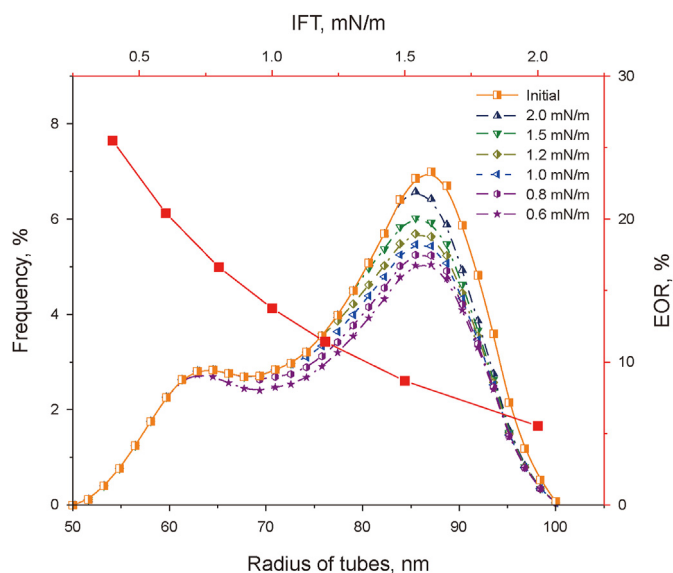
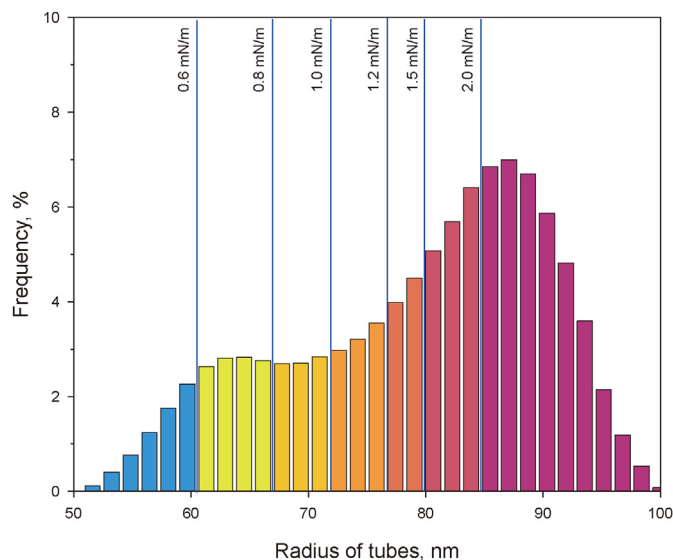**Fig. 10.** Oil distribution among pores with different radii.

Fig. 11. The relationship between interfacial tension and the minimum pore radius for oil mobility.

pores, as shown in Fig. 8(d).

5. Conclusions

The establishment of the mathematical model of the ICB in this paper considers the impact of cross-flow between tubes and adopts the pressure balance assumption (Dong et al., 2005) to describe the cross-flow. Moreover, the position of the leading front is not explicitly defined in the establishment of the mathematical model. Rather, the physical phenomenon of multiphase flow in porous media (tight rocks) is leveraged to capture the realistic imbibition behavior within various pores. Finally, a mathematical model of ICBs that incorporates the effects of viscosity, interfacial tension, and wettability is developed. Using the established mathematical

model, the effects of viscosity ratio and wettability on the leading front and displacement front shape, as well as the impact of interfacial tension on the oil recovery and the minimum pore size for oil flow, are analyzed.

(1) Compared to other mathematical models that describe the imbibition behavior in the ICB, the new one proposed in this study considers the impact of wettability and viscosity ratio, thereby achieving better agreement with the experimental outcomes of the experiments of liquid-displacing-gas and water-displacing-oil in porous media (including natural rocks and microfluidic chips). The calculation results of the new model show that when a more-viscous wetting fluid is used as the displacing phase, the displacing phase is first invaded into the smallest diameter tube; as the imbibition progresses, the displacing phase gradually enters tubes with increasing diameter. Conversely, when a less-viscous wetting fluid is used as the displacing phase, the displacing phase is first invaded into the largest diameter tube, and as the imbibition progresses, it gradually enters tubes with decreasing diameter. When a non-wetting fluid is used as the displacing phase, the invasion order of the displacing phase under different viscosity ratio conditions will also vary.

(2) The new model can predict imbibition behavior and changes in water saturation profiles during displacement in porous media. In addition, it can also predict the influence of interfacial tension on the minimum tube size for oil flow and the imbibition rate in different tubes. The results indicate that the reduction of interfacial tension can narrow the oil–water two-phase region, leading to a water saturation profile that is closer to piston-like displacement. Additionally, the reduction of interfacial tension can also decrease the minimum tube size for oil flow, allowing more oil to be mobilized in the tubes and thus enhancing oil recovery.

(3) The new model not only provides a prediction method for the distribution of the residual oil (in pores of different sizes) and the mobilization of oil in different pores, but also for the recovery efficiency after tight rock oil displacement.

CRediT authorship contribution statement

Wen-Quan Deng: Writing − original draft, Validation, Methodology, Investigation, Data curation. **Tian-Bo Liang:** Writing − review & editing, Validation, Supervision, Funding acquisition. **Wen-Zhong Wang:** Software, Data curation. **Hao Liu:** Investigation, Data curation. **Jun-Lin Wu:** Investigation, Data curation. **Fu-Jian Zhou:** Writing − review & editing, Supervision.

References

Adenutsi, C.D., Li, Z., Xu, Z., Sun, L., 2019. Influence of net confining stress on NMR T_2 distribution and two-phase relative permeability. J. Petrol. Sci. Eng. 178, 766–777. https://doi.org/10.1016/j.petrol.2019.03.083.

Ashraf, S., Méheust, Y., Phirani, J., 2023. Spontaneous imbibition dynamics in two-dimensional porous media: a generalized interacting multi-capillary model. Phys. Fluids 35, 012005. https://doi.org/10.1063/5.0123229.

Ashraf, S., Visavale, G., Bahga, S.S., Phirani, J., 2017. Spontaneous imbibition in parallel layers of packed beads. Eur. Phys. J. E. 40, 39. https://doi.org/10.1140/epje/i2017-11530-8.

Bico, J., Quéré, D., 2003. Precursors of impregnation. EPL 61, 348–353. https://doi.org/10.1209/epl/i2003-00196-9.

Carrell, C., Kava, A., Nguyen, M., Menger, R., Munshi, Z., Call, Z., Nussbaum, M., Henry, C., 2019. Beyond the lateral flow assay: a review of paper-based microfluidics. Microelectron. Eng. 206, 45–54. https://doi.org/10.1016/j.mee.2018.12.002.

Chen, H., Chen, K., Yang, M., Xu, P., 2020. A fractal capillary model for multiphase flow in porous media with hysteresis effect. Int. J. Multiphas. Flow 125, 103208. https://doi.org/10.1016/j.ijmultiphaseflow.2020.103208.

Chen, H., Guan, J., Fang, W., 2012. Microscopic mechanism of periodical electroosmosis in reservoir rocks. Appl. Math. Mech.-Engl. Ed. 33, 1275–1286. https://doi.org/10.1007/s10483-012-1621-9.

Dahle, H.K., Celia, M.A., Majid Hassanizadeh, S., 2005. Bundle-of-tubes model for calculating dynamic effects in the capillary-pressure- saturation relationship. Transp. Porous Med. 58, 5–22. https://doi.org/10.1007/s11242-004-5466-4.

Dong, M., Dullien, F.A.L., Zhou, J., 1998. Characterization of waterflood saturation profile histories by the 'Complete' capillary number. Transport Porous Media 31, 213–237. https://doi.org/10.1023/A:1006565621860.

Dong, M., Dullien, F.A.L., Dai, L., Li, D., 2006. Immiscible displacement in the interacting capillary bundle model Part II. Applications of model and comparison of interacting and non-interacting capillary bundle models. Transp. Porous Med. 63, 289–304. https://doi.org/10.1007/s11242-005-6530-4.

Dong, M., Dullien, F.A.L., Dai, L., Li, D., 2005. Immiscible displacement in the interacting capillary bundle model Part I. Development of interacting capillary bundle model. Transp. Porous Med. 59, 1–18. https://doi.org/10.1007/s11242-004-0763-5.

Gao, H., Wang, Y., Xie, Y., Ni, J., Li, T., Wang, C., Xue, J., 2021. Imbibition and oil recovery mechanism of fracturing fluids in tight sandstone reservoirs. ACS Omega 6, 1991–2000. https://doi.org/10.1021/acsomega.0c04945.

Gaol, C.L., Wegner, J., Ganzer, L., 2020. Real structure micromodels based on reservoir rocks for enhanced oil recovery (EOR) applications. Lab Chip 20, 2197–2208. https://doi.org/10.1039/D0LC00257G.

Gharibshahi, R., Omidkhah, M., Jafari, A., Fakhroueian, Z., 2020. Hybridization of superparamagnetic Fe_3O_4 nanoparticles with MWCNTs and effect of surface modification on electromagnetic heating process efficiency: a microfluidics enhanced oil recovery study. Fuel 282, 118603. https://doi.org/10.1016/j.fuel.2020.118603.

Gostick, J.T., 2017. Versatile and efficient pore network extraction method using marker-based watershed segmentation. Phys. Rev. E. 96, 023307. https://doi.org/10.1103/PhysRevE.96.023307.

Gu, X., Pu, C., Huang, H., Huang, F., Li, Y., Liu, Y., Liu, H., 2017. Micro-influencing mechanism of permeability on spontaneous imbibition recovery for tight sandstone reservoirs. Petrol. Explor. Dev. 44, 1003–1009. https://doi.org/10.1016/S1876-3804(17)30112-X.

Guo, J., Li, M., Chen, C., Tao, L., Liu, Z., Zhou, D., 2020. Experimental investigation of spontaneous imbibition in tight sandstone reservoirs. J. Petrol. Sci. Eng. 193, 107395. https://doi.org/10.1016/j.petrol.2020.107395.

Hou, X., Sheng, J.J., 2022. Experimental study on the imbibition mechanism of the Winsor type I surfactant system with ultra-low IFT in oil-wet shale oil reservoirs by NMR. J. Petrol. Sci. Eng. 216, 110785. https://doi.org/10.1016/j.petrol.2022.110785.

Hussain, S.T., Rahman, S.S., Azim, R.A., Haryono, D., Regenauer-Lieb, K., 2021. Multiphase fluid flow through fractured porous media supported by innovative laboratory and numerical methods for estimating relative permeability. Energy Fuels 35, 17372–17388. https://doi.org/10.1021/acs.energyfuels.1c01313.

Johannessen, A.M., Spildo, K., 2013. Enhanced oil recovery (EOR) by combining surfactant with low salinity injection. Energy Fuels 27, 5738–5749. https://doi.org/10.1021/ef400596b.

Kathel, P., Mohanty, K.K., 2013. EOR in tight oil reservoirs through wettability alteration. In: SPE Annual Technical Conference and Exhibition. https://doi.org/10.2118/166281-MS.

Kelly, S., Torres-Verdín, C., Balhoff, M.T., 2018. Influences of polarity and hydration cycles on imbibition hysteresis in silica nanochannels. Phys. Chem. Chem. Phys. 20, 456–466. https://doi.org/10.1039/C7CP05833K.

Lai, F., Li, Z., Wei, Q., Zhang, T., Zhao, Q., 2016. Experimental investigation of spontaneous imbibition in a tight reservoir with nuclear magnetic resonance testing. Energy Fuels 30, 8932–8940. https://doi.org/10.1021/acs.energyfuels.6b01324.

Lala, A.M.S., El-sayed, N.A.E.-A., 2015. The application of petrophysics to resolve fluid flow units and reservoir quality in the Upper Cretaceous Formations: Abu Sennan oil field, Egypt. J. Afr. Earth Sci. 102, 61–69. https://doi.org/10.1016/j.jafrearsci.2014.10.018.

Lee, K.K., Kim, M.-O., Choi, S., 2019. A whole blood sample-to-answer polymer lab-on-a-chip with superhydrophilic surface toward point-of-care technology. J. Pharmaceut. Biomed. Anal. 162, 28–33. https://doi.org/10.1016/j.jpba.2018.09.007.

Lei, W., Lu, X., Wang, M., 2023. Multiphase displacement manipulated by micro/nanoparticle suspensions in porous media via microfluidic experiments: from interface science to multiphase flow patterns. Adv. Colloid Interface Sci. 311, 102826. https://doi.org/10.1016/j.cis.2022.102826.

Li, G., Liu, C., Zhou, Y., Wu, H., Awan, R.S., Shi, F., Wu, Y., Zang, Q., Wu, Y., 2023. Controlling effects of pore-throat structure and fractal characteristics on the physical properties of ultra-low permeability sandstone reservoirs: a case study of the sixth member of the Yanchang Formation in the Xiaojiahe area, Ordos Basin. Geol. J. 58, 1945–1964. https://doi.org/10.1002/gj.4700.

Li, S., Dong, M., Luo, P., 2017. A crossflow model for an interacting capillary bundle: development and application for waterflooding in tight oil reservoirs. Chem. Eng. Sci. 164, 133–147. https://doi.org/10.1016/j.ces.2017.01.059.

Liang, B., Jiang, H., Li, J., Gong, C., Jiang, R., Qu, S., Pei, Y., Yang, H., 2017. Investigation of oil saturation development behind spontaneous imbibition front using nuclear magnetic resonance T_2. Energy Fuels 31, 473–481. https://doi.org/10.1021/acs.energyfuels.6b02903.

Liu, Y., Kaszuba, J., Oakey, J., 2019. Microfluidic investigations of crude oil-brine interface elasticity modifications via brine chemistry to enhance oil recovery. Fuel 239, 338–346. https://doi.org/10.1016/j.fuel.2018.11.040.

Lu, Z., Liu, C., Zang, Q., Wu, Y., Yang, X., Yang, H., Zeng, X., Li, W., 2022. Application of high pressure mercury injection and nuclear magnetic resonance in analysis of the pore structure of dense sandstone: a case study of the Heshui area, Ordos Basin. Bull. Geol. Sci. Technol. 41 (3), 300–310. https://doi.org/10.19509/j.cnki.dzkq.2021.0256 (in Chinese).

Lyu, C., Ning, Z., Cole, D.R., Wang, Q., Chen, M., 2020. Experimental investigation on T_2 cutoffs of tight sandstones: comparisons between outcrop and reservoir cores. J. Petrol. Sci. Eng. 191, 107184. https://doi.org/10.1016/j.petrol.2020.107184.

Lyu, C., Ning, Z., Wang, Q., Chen, M., 2018. Application of NMR T_2 to pore size distribution and movable fluid distribution in tight sandstones. Energy Fuels 32, 1395–1405. https://doi.org/10.1021/acs.energyfuels.7b03431.

Mason, G., Morrow, N.R., 2013. Developments in spontaneous imbibition and possibilities for future work. J. Petrol. Sci. Eng. 110, 268–293. https://doi.org/10.1016/j.petrol.2013.08.018.

Matthews, G.P., Canonville, C.F., Moss, A.K., 2006. Use of a void network model to correlate porosity, mercury porosimetry, thin section, absolute permeability, and NMR relaxation time data for sandstone rocks. Phys. Rev. E 73, 031307. https://doi.org/10.1103/PhysRevE.73.031307.

Meng, Z., Yang, S.-L., Cui, Y., Zhong, Z.-Y., Wang, L., Qian, K., Ma, Q.-Z., Wang, J.-R., 2018. Enhancement of the imbibition recovery by surfactants in tight oil reservoirs. Petrol. Sci. 15, 783–793. https://doi.org/10.1007/s12182-018-0253-y.

Nelson, P.H., 2009. Pore-throat sizes in sandstones, tight sandstones, and shales. Bulletin 93, 329–340. https://doi.org/10.1306/10240808059.

Nemer, M.N., Rao, P.R., Schaefer, L., 2020. Wettability alteration implications on pore-scale multiphase flow in porous media using the lattice Boltzmann method. Adv. Water Resour. 146, 103790. https://doi.org/10.1016/j.advwatres.2020.103790.

Pak, T., Rabbani, H.S., Qaseminejad Raeini, A., Shokri, N., 2023. Effects of the pore morphology on multiphase fluid displacement in porous media–A high-resolution modeling investigation. ACS Omega 8, 3889–3895. https://doi.org/10.1021/acsomega.2c06295.

Qin, C.-Z., Wang, X., Zhang, H., Hefny, M., Jiang, H., Tian, J., Deng, W., 2022. Numerical studies of spontaneous imbibition in porous media: model development and pore-scale perspectives. J. Petrol. Sci. Eng. 218, 110961. https://doi.org/10.1016/j.petrol.2022.110961.

Rich, M., Mohd, O., Ligler, F.S., Walker, G.M., 2019. Characterization of glass frit capillary pumps for microfluidic devices. Microfluid. Nanofluidics 23, 70. https://doi.org/10.1007/s10404-019-2238-6.

Sun, Y., Kharaghani, A., Tsotsas, E., 2016. Micro-model experiments and pore network simulations of liquid imbibition in porous media. Chem. Eng. Sci. 150, 41–53. https://doi.org/10.1016/j.ces.2016.04.055.

Thompson, W.H., 2018. Perspective: dynamics of confined liquids. J. Chem. Phys. 149, 170901. https://doi.org/10.1063/1.5057759.

Unsal, E., Mason, G., Ruth, D.W., Morrow, N.R., 2007. Co- and counter-current spontaneous imbibition into groups of capillary tubes with lateral connections permitting cross-flow. J. Colloid Interface Sci. 315, 200–209. https://doi.org/10.1016/j.jcis.2007.06.070.

Wang, J., Dong, M., 2011. Trapping of the non-wetting phase in an interacting triangular tube bundle model. Chem. Eng. Sci. 66, 250–259. https://doi.org/10.1016/j.ces.2010.10.009.

Wang, J., Dullien, F.A.L., Dong, M., 2008. Fluid transfer between tubes in interacting capillary bundle models. Transp. Porous Med. 71, 115–131. https://doi.org/10.1007/s11242-007-9115-6.

Washburn, E.W., 1921. The dynamics of capillary flow. Phys. Rev. 17, 273–283. https://doi.org/10.1103/PhysRev.17.273.

Wijaya, N., Sheng, J.J., 2020. Mitigating near-fracture blockage and enhancing oil recovery in tight reservoirs by adding surfactants in hydraulic fracturing fluid. J. Petrol. Sci. Eng. 185, 106611. https://doi.org/10.1016/j.petrol.2019.106611.

Wolf, F.G., Siebert, D.N., Carreño, M.N.P., Lopes, A.T., Zabot, A.M., Surmas, R., 2022.

Dual-porosity micromodels for studying multiphase fluid flow in carbonate rocks. Lab Chip 22, 4680—4692. https://doi.org/10.1039/D2LC00445C.

Wu, Y., Tahmasebi, P., Lin, C., Ren, L., Zhang, Y., 2020. Quantitative characterization of non-wetting phase in water-wet porous media based on multiphase flow experiment and numerical simulation. J. Petrol. Sci. Eng. 188, 106914. https://doi.org/10.1016/j.petrol.2020.106914.

Xiong, Y., Yu, J., Sun, H., Yuan, J., Huang, Z., Wu, Y., 2017. A new non-Darcy flow model for low-velocity multiphase flow in tight reservoirs. Transp. Porous Med. 117, 367—383. https://doi.org/10.1007/s11242-017-0838-8.

Yan, J., Li, Y., Xie, X., Slaný, M., Dong, S., Wu, Y., Chen, G., 2023. Research of a novel fracturing-production integral fluid based on cationic surfactant. J. Mol. Liq. 369, 120858. https://doi.org/10.1016/j.molliq.2022.120858.

Yang, D., Currier, R.P., Zhang, D.Z., 2009. Ensemble phase averaged equations for multiphase flows in porous media. Part 1: the bundle-of-tubes model. Int. J. Multiphas. Flow 35, 628—639. https://doi.org/10.1016/j.ijmultiphaseflow.2009.03.002.

Yang, Z., Liu, X., Li, H., Lei, Q., Luo, Y., Wang, X., 2019. Analysis on the influencing factors of imbibition and the effect evaluation of imbibition in tight reservoirs. Petrol. Explor. Dev. 46, 779—785. https://doi.org/10.1016/S1876-3804(19)60235-1.

Yuan, L., Habibi, A., Dehghanpour, H., 2021. Liquid imbibition in tight rocks: the role of disjoining pressure. Colloids Surf. A Physicochem. Eng. Asp. 627, 127037. https://doi.org/10.1016/j.colsurfa.2021.127037.

Zhang, Q., Chen, W., Wu, G., Wang, W., Du, Y., Bi, J., 2022. Effect of PVA-treated soil on water-salt capillary rise in loess soil: soil column experiment. J. Hydrol. 610, 127806. https://doi.org/10.1016/j.jhydrol.2022.127806.

Zhao, J., Huang, Z., Zhang, J., Deng, G., Xu, M., 2022. Pore structure fractal and graded evaluation in tight sandstone reservoirs: a case study of the Huangliu Formation in the Ledong. Acta Sedimentol. Sin. 1—19. https://doi.org/10.14027/j.issn.1000-0550.2022.038 (in Chinese).

Zhao, L., Jiang, H., Wang, H., Yang, H., Sun, F., Li, J., 2020. Representation of a new physics-based non-Darcy equation for low-velocity flow in tight reservoirs. J. Petrol. Sci. Eng. 184, 106518. https://doi.org/10.1016/j.petrol.2019.106518.

Zhao, M., Liu, S., Gao, Z., Wu, Y., Dai, C., 2022. The spontaneous imbibition mechanisms for enhanced oil recovery by gel breaking fluid of clean fracturing fluid. Colloids Surf. A Physicochem. Eng. Asp. 650, 129568. https://doi.org/10.1016/j.colsurfa.2022.129568.

Zhou, Y., Helland, J.O., Hatzignatiou, D.G., 2013. Pore-scale modeling of water-flooding in mixed-wet-rock images: effects of initial saturation and wettability. SPE J. 19, 88—100. https://doi.org/10.2118/154284-PA.

Zou, A., Poudel, S., Gupta, M., Maroo, S.C., 2021. Disjoining pressure of water in nanochannels. Nano Lett. 21, 7769—7774. https://doi.org/10.1021/acs.nanolett.1c02726.

Zou, C., Yang, Z., Tao, S., Li, W., Wu, S., Hou, L., Zhu, R., Yuan, X., Wang, L., Gao, X., Jia, J., Guo, Q., 2012. Nano-hydrocarbon and the accumulation in coexisting source and reservoir. Petrol. Explor. Dev. 39, 15—32. https://doi.org/10.1016/S1876-3804(12)60011-1.